Effect of surface topography on anisotropic friction of graphene layers

M. Ding, Y. Cong, R. Li, F. Xu

Effect of surface topography on anisotropic friction of graphene layers

Mingda Ding[a], **Yu Cong**[b], **Ruiyang Li**[a], **Fan Xu**[a,1]

[a]Institute of Mechanics and Computational Engineering, Department of Aeronautics and Astronautics, Fudan University, 220 Handan Road, Shanghai 200433, P.R. China
[b]Université Paris-Saclay, Univ Evry, LMEE, 91020, Evry, France

Abstract

Tribological behavior of graphene layers has been a focus of intensive research interest since its crystal lattice structure can be exploited to achieve incommensurate contact, leading to nearly zero friction, namely structural superlubricity. However, wrinkling undulations are omnipresent on graphene and difficult to be completely eliminated, which inevitably resists superlubricity in reality. Here, we explore how the presence of surface wrinkles affects nanotribological behavior of graphene sliding systems. Using a dimensionless parameter based on the topographic geometry, we propose a set of quantitative criteria permitting incommensurate-induced low friction even superlubricity to retain, despite the presence of surface wrinkles. Failing the criteria, achievement of superlubricity on wrinkled surface becomes implausible with unfavourable anisotropy and considerable friction. Besides, we examine the influence of diverse spatial topographic patterns such as stripe, checkerboard and herringbone on tribological behavior, and reveal that surface wrinkles can precisely tune the oscillating undulation of friction response. The proposed criteria may serve as an indicative reference that allows predicting the state of friction on practical, wrinkled graphene, and eventually assist the design of nanotribological systems with tunable friction.

Keywords: Graphene; Superlubricity; Friction; Wrinkles; Topographic pattern.

1 Introduction

Graphene layers, as exceptional solid lubricant to achieve friction and wear reduction in modern miniaturized electromechanical applications, are gaining increasing attention and widely investigated in nanotribology as a promising candidate to form sliding junctions, notably in the context of structural superlubricity (Hod et al., 2018). The concept "superlubricity", first mentioned three decades ago (Hirano et al., 1991), refers to a regime of quasi frictionless sliding (in practice, friction coefficient $< 10^{-3}$ according to Martin et al. (1993) exclusively based on the maintenance of incommensurate contact of crystalline surfaces during relative motion. The mechanism behind it relies on the lattice mismatch of the contacting crystal lattices, which creates incommensurate positioning of potential energy of surface atoms, leading to the suppression of friction forces. Such regulation that friction reduces with increasing mismatch angle from 0° to 30° is also recognized as "anisotropy friction" (Hirano and Shinjo, 1993). Since the pioneering experimental work of Dienwiebel et al. (2004), Socoliuc et al. (2004) and Liu et al. (2012), in which nano- and micro-scale superlubricity was successively confirmed,

[1]Corresponding author.
E-mail address: fanxu@fudan.edu.cn (F. Xu).

substantial effort has been undertaken to expand superlubricity to a greater scale with significance for macroscopic applications. In this regard, several inherent issues of structural superlubricity have to be addressed. We note in particular its high level of friction anisotropy (Wang et al., 2019), for which a few heterojunction based solutions have been proposed (Leven et al., 2012; Mandelli et al., 2017; Wang et al., 2014). The best understood strategies, however, still rely on homogeneous graphene systems due to their wide accessibility in fabrication and laboratory manipulation. Furthermore, recent theoretical (Wang et al., 2019a,b) and experimental (Zhang et al., 2019) works addressed the problem of friction anisotropy of graphene sliding systems (Bonelli et al., 2009; de Wijn et al., 2010; Filippov et al., 2008), which makes graphene a promising candidate for achieving superlubricity in a larger scale.

To fulfill the potential of graphene sliding systems for macroscale superlubricity, one has to gain a thorough understanding of their frictional behaviors under realistic conditions. Graphene, like many other 2D materials, is inherently unstable in its free configuration, and tends to form out-of-plane deformations (Meyer et al., 2007) such as wrinkles (Deng and Berry, 2016). This intrinsic property can be observed both on graphene obtained from exfoliation process (Choi et al., 2011), and from those formed by chemical vapor deposition (CVD) (Obraztsov et al., 2007; Paronyan et al., 2011). Wrinkles naturally formed on graphene tend to remain (Cho et al., 2013), some may even move on the graphene surface under particular thermal conditions (Guo and Guo, 2013), and become difficult to be eliminated in large scale. However, knowledge on the implications of wrinkles on the friction of graphene is limited to the qualitative level (Almeida et al., 2016; Choi et al., 2011; Li et al., 2014; Smolyanitsky, 2015). It is therefore important to gain a quantitative understanding for achieving realistic superlubricity using graphene systems. From this perspective, we conduct our investigation by considering the sliding of a graphene flake on the top of a wrinkled graphene substrate. The graphene slider is of varying dimensions, and the substrate exhibits a variety of wrinkling topography. The friction simulation is performed by considering evolving crystal lattice mismatches, which allows us to explore the effect of wrinkles on the friction anisotropy, especially the incommensurate-induced superlubricity. Moreover, we examine geometric characteristics of the wrinkle such as wavelength, amplitude and topographic patterns. Our results can help predict nanotribological behaviors of wrinkled graphene, and assist the scaling up effort of superlubricity with the perspective to achieve realistic applications.

2 Model

On the bilayer graphene sliding system. We investigate interlayer frictions by considering the sliding motion of a hexagonal monolayer graphene flake on top of a rectangular graphene ribbon substrate with varying wave undulations (see Fig. 1). We apply constant force F_N (nN/atom) to each atom of the graphene slider along the negative out-of-plane z direction, which corresponds to the normal load in the friction process. Then, inspired by Zhang et al. (2015) and Wang et al. (2019a), we implement sliding motion of the flake by connecting its centroid to a virtual atom with a linear spring of stiffness k_{link}. While the virtual atom is pulled to advance at constant velocity v_{pull} along the x direction, the connecting spring drives the flake to follow up. The pulling velocity induced lateral driving force F_{ptot} from the spring is equally distributed to each atom of the flake, given by

$$F_{\text{patom}} = \frac{F_{\text{ptot}}}{N_{\text{atom}}} = \frac{k_{\text{link}}\left(x_{\text{pull}} - x_{\text{c}} - l_0\right)}{N_{\text{atom}}}, \tag{1}$$

where N_{atom} is the number of atoms in the flake, x_{pull} and x_{c} represent the position of virtual atom and the centroid of flake, respectively. The unstretched length of the spring is set as $l_0 = 30$ Å in simulations. In order to focus on the reactions due to frictions alone, we constrain displacements of the flake atoms in the y direction, normal to the sliding motion. We prevent in this way the rotational

and lateral deviations of the flake. We do not constrain the flake atoms in the z direction so as to allow free out-of-plane deformation when it slides on the substrate under the effect of its uneven energy surface. Moreover, we prescribe substrates of varying geometric configuration, while for each given setup, we consider it to be rigid and fully constrain its degrees of freedom to make sure the system behaves precisely in response to the desired wrinkling topography.

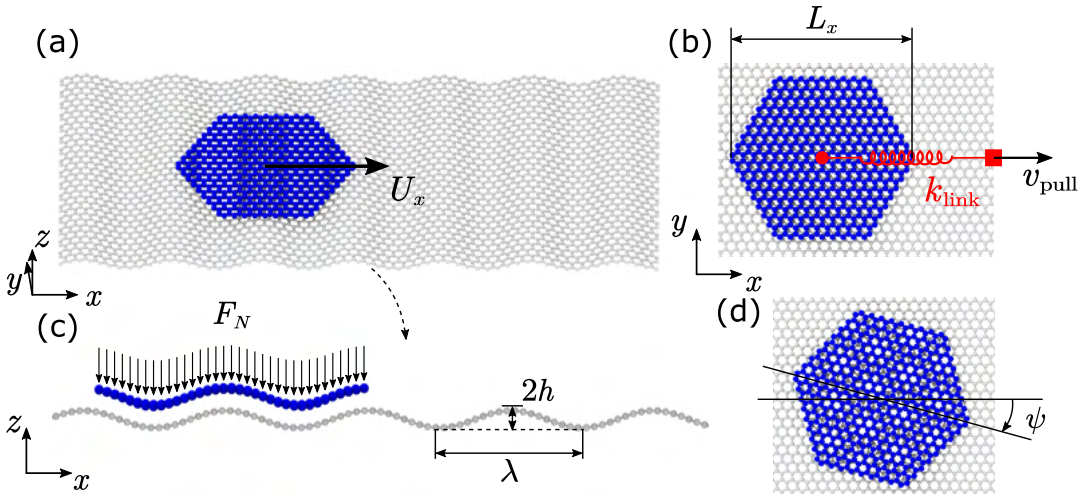

Figure 1: Schematic of computational model. (a) A hexagonal graphene flake is placed on a rectangle graphene substrate and tracked to move along the x-axis direction. (b) The flake size is characterized by the distance between two opposite vertices L_x. The flake is tracked by a spring with the stiffness $k_{\text{link}} = 36.3$ N/m. (c) The normal force F_N is applied to each flake atom sliding on a wavy graphene layer with amplitude H and wavelength λ. (d) The mismatch angle ψ between the flake and substrate.

On the graphene substrate. We prescribe different wrinkling patterns to the substrate graphene so that it presents diverse wavy fluctuations. Notably, the zigzag direction of the substrate graphene is aligned along x axial. With wavelength λ and amplitude h (see Fig. 1(c)), the sinusoidal undulating surface can be built by $z = h\sin(2\pi x/\lambda)$. Other topographic patterns including checkerboard ($z = h\cos(2\pi x/\lambda)\cos(2\pi y/\lambda)$) and herringbone ($z = h/\sqrt{2}\cdot[\cos(2\pi x/\lambda) + \sin(2\pi x/\lambda)\cos(2\pi y/\lambda)]$) are taken into account as well.

On the graphene slider. The slider flake is composed of a regular hexagonal graphene monolayer. We use L_x to denote its characteristic size which refers to the distance between two opposite vertices of the hexagon (see Fig. 1(b)). We choose hexagonal graphene flakes since their boundaries do not present free atoms or chemical bonds compared with the rectangular counterparts. Furthermore, benefiting from its 60° rotational symmetry, hexagon is intrinsically consistent with the symmetry of the graphene lattice, whereas in contrast, rectangular graphene has to be twisted for 180° to coincide with its initial configuration.

On the design of simulation cases. To investigate the influence on friction anisotropy due to flake-substrate lattice mismatch, we prescribe for each wrinkled substrate setup, a range of simulations with varying mismatch angles ψ from 0° to 30° at an interval of 5°. Here $\psi = 0°$ indicates that the relative position between the flake and substrate in $x - y$ plane corresponds to AB stacking for commensurate state. The flake with a mismatch angle ψ is then generated from such AB stacking by rotating the flake around z axis with centroid as the center. The range of ψ covers both commensurate and incommensurate contacts, allowing us to examine precisely the effect on the regime of superlubricity.

Simulation specifications. Intralayer C-C interactions are modelled using AIREBO force field (Stuart et al., 2000). Non-bonded interlayer interactions are modelled by standard Lennard-Jones (LJ) 12-6

potential (Lennard-Jones, 1931): $V_{LJ}^{12-6}(r) = 4\varepsilon[(\sigma/r)^{12} - (\sigma/r)^6]$, evaluated on each pair of atoms governed by van der Waals interaction, where r is the distance between the two atoms, ε the energy well depth, and σ the equilibrium distance. We choose LJ potential for both its capacity of representing the friction anisotropy (Pan et al., 2019), and its higher computational efficiency given the extensive amount of cases needed for this study. Here we take the following parameter setup: $\varepsilon = 2.968$ meV, $\sigma = 3.407$ Å, and cutoff length $L_{\text{cutoff}} = 10$ Å, so as to limit LJ atom pair calculations to short range interactions. The simulations were carried out using LAMMPS (Plimpton, 1995), under constant temperature $T = 1$ K maintained via Nosé-Hoover thermostat. Here we took the low simulating temperature to exclude the effect of atomic thermal fluctuation, and obtain a stable relation between friction and substrate undulation. Prior to applying pulling actions to the graphene flake, the system left to relax with the normal pressure $F_N = 0.2$ nN/atom activated, for equilibrium at constant NVE (number, volume and energy) during 20 ps. Then, sliding motion is introduced by prescribing constant velocity $v_{\text{pull}} = 10$ m/s to the virtual pulling atom and the spring constant $k_{\text{link}} = 36.3$ N/m. Effects of spring constant on friction response are quantitatively examined in Supplementary Material and a moderate parameter is accounted to prevent the stick-slip behavior induced by substrate undulation. Due to timescale limitations of molecular dynamics, the implemented sliding velocity is significantly faster than experimental conditions (Wang et al., 2019), but it still remains admissible for the system to capture stick-slip behavior (Liu, 2014; Ouyang et al., 2018). We have examined in Supplementary Material the velocity varying from 5 m/s to 15 m/s, which demonstrates that the friction response remains unchanged.

Friction force extraction. Since instantaneous friction force is not constant, a rational value is necessary to indicate the friction profile throughout the substrate. We first define the friction $F_x(U_x)$ as a function of the sliding displacement U_x, and the friction F_x (nN/atom) in each frame is calculated by averaging the total friction over the atom number of the flake. In MD simulation, the total friction is calculated by extracting and summing up the force between all the atoms in the substrate and flake. Notably, we define the $F_x(U_x) > 0$ when the flake receives a resistant force along negative x direction from the substrate. To evaluate the friction during the whole sliding process, the considered average friction F_f is obtained by averaging the energy dissipation ΔW over the sliding period Δx (van Wijk et al., 2013), which indicates the work of the resistant force ($F_x(U_x) > 0$). Hence, the average force can be expressed as

$$F_f = \frac{\Delta W}{\Delta x} = \int_{\Delta x} \frac{(F_x(U_x) + |F_x(U_x)|)}{2\Delta x} \mathrm{d}U_x. \tag{2}$$

Since the friction force is periodic during the sliding process, we take Δx as an integer multiple of the friction period (integer number of waves) when calculating F_f.

3 Results and discussion

3.1 Anisotropic friction on wrinkled graphene

We first present our investigation procedure with a typical group of flake-substrate systems. Here, the wrinkles are formed by sinusoidal undulations of amplitudes $h = 0$ Å, 0.4 Å, 0.8 Å and 1.2 Å, and fixed wavelength $\lambda = 31.7$ Å. The characteristic length of flake is $L_x = 41.8$ Å. To examine the anisotropic friction, we perform simulations with evolving mismatch angles ψ from 0° to 60° at an interval of 5°. In total, a set of 52 simulations of distinct substrate wrinkles and lattice mismatch are carried out. We confront results from each wrinkled topography to the case with plane substrate ($h = 0$ Å). Their comparison let appear the effect on anisotropic friction exclusively caused by substrate undulations. Figure 2 demonstrates the evolving friction behavior as a result of the wrinkled substrate,

where contact incommensuration occurs in the range of lattice mismatch $\psi \in [10°,\ 50°]$ and thus superlubric sliding is achieved on plane surface (blue curve in Fig. 2). Note that each solution point in Fig. 2 is calculated using Eq. (2) based on instantaneous friction forces computed during the sliding process. We observe degraded lubricating effect (red, azure and purple curves) caused by the substrate undulation, which increases with the wrinkling amplitude. This let us estimate a tolerance threshold based on h for the given wrinkling wavelength $\lambda = 31.7$ Å, which allows the system to approximate superlubricity despite the substrate roughness.

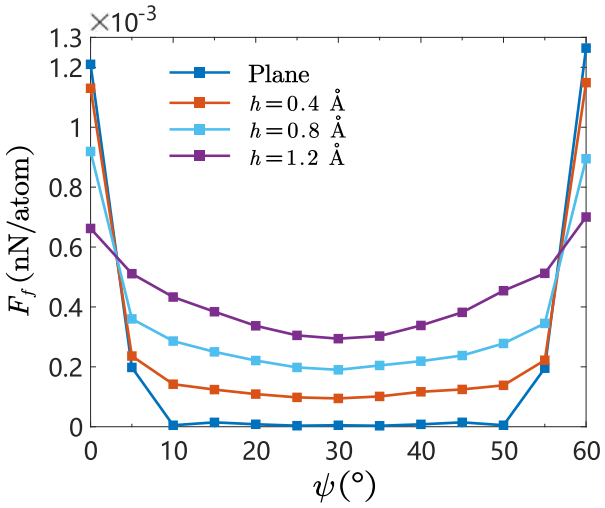

Figure 2: Friction force *v.s.* mismatch angle for both flat and wrinkled substrates. Wrinkles follow sinusoidal undulations of wavelength $\lambda = 31.7$ Å and amplitudes $h = 0.4$ Å (red), 0.8 Å (azure) and 1.2 Å (purple). The characteristic length of the slider flake $L_x = 41.8$ Å. It can be observed significant lubricating effect in the wrinkled cases due to mismatch angle, whereas it appears degraded trend with the rise of wrinkling amplitude, compared with flat superlubric sliding.

Interestingly, we reveal weaker frictional resistance in wrinkled cases compared with their plane counterpart in the regions near $\psi = 0°$ and $\psi = 60°$ which refer to commensurate friction. We find that surface wrinkles reduce commensurate friction in these regions. This phenomenon can be explained by the localized and reduced contact area due to wrinkled contact interface. However, this phenomenon is temporary and vanishes as soon as contact incommensuration is confirmed.

We next show examples of the instantaneous friction forces obtained respectively from a plane and a wrinkled graphene of wavelength $\lambda = 31.7$ Å. Details of the oscillating friction force is plotted in Fig. 3. On the left column, friction forces are periodic with the wavelength ~ 2.46 Å corresponding to the graphene lattice constant along x direction (zigzag, $1.42 \times \sqrt{3}$ Å). On the right column, friction forces can be viewed as the combination of a short-wavelength fluctuation plus a long-wavelength fluctuation. The former one is composed of short waves of the same wavelength (~ 2.46 Å) as those on the left column, which originates from the high frequency, cross-lattice (stick-slip) movement of the graphene lattice during the sliding process. The latter, is composed of long waves produced when the graphene flake slides on the substrate undulations.

3.2 Size effect

Wavelength and amplitude. We explore the size effect of varying geometry attributes of wrinkles such as wave density (wavelength) and height (amplitude) on the anisotropic friction behavior. Figure 4 illustrates 189 simulation cases based on 9 different wavelengths $\lambda = 9.7$ Å, 21.8 Å, 26.8 Å, 29.3 Å,

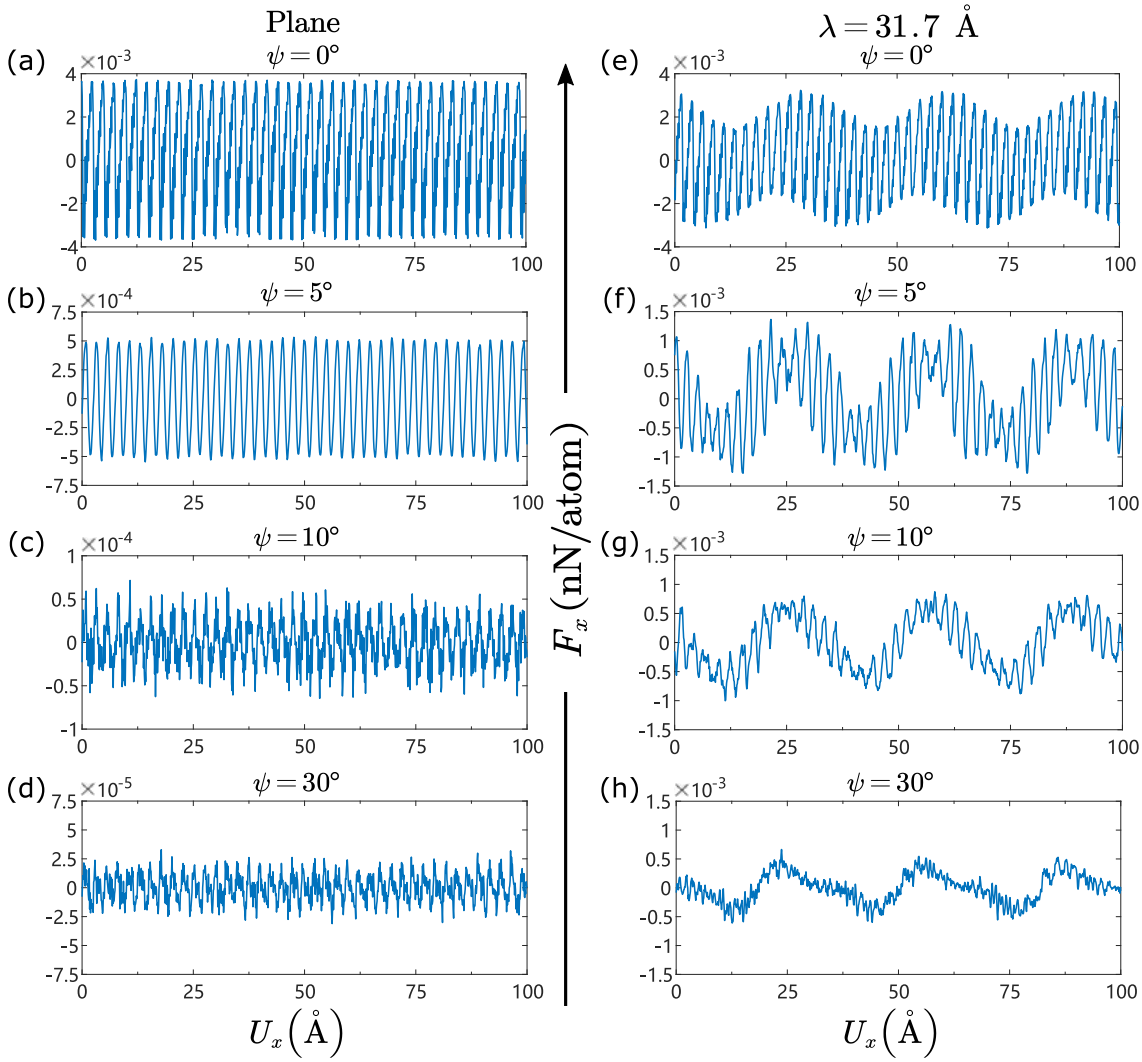

Figure 3: Oscillating, instantaneous friction forces of the flakes on plane (a-d) and wrinkled substrate (e-h) with different lattice mismatch angles $\psi = 0°$, $5°$, $10°$ and $30°$.

31.7 Å, 34.2 Å, 36.7 Å, 41.6 Å, and 61.4 Å. For each wavelength, we consider 4 different amplitudes $h = 0$ Å (blue), 0.4 Å (red), 0.8 Å (azure) and 1.2 Å (purple). On each of the 36 substrate setups, we examine the friction anisotropy by considering 7 mismatch angles ranging from 0° to 30°. Friction behaviors on mismatch angles from 30° to 60° are identical to those computed in the range [0°, 30°] due to symmetry of the hexagonal flake. Here, we apply the same graphene flake to the cases, and will examine the dependence on flake size in the next section.

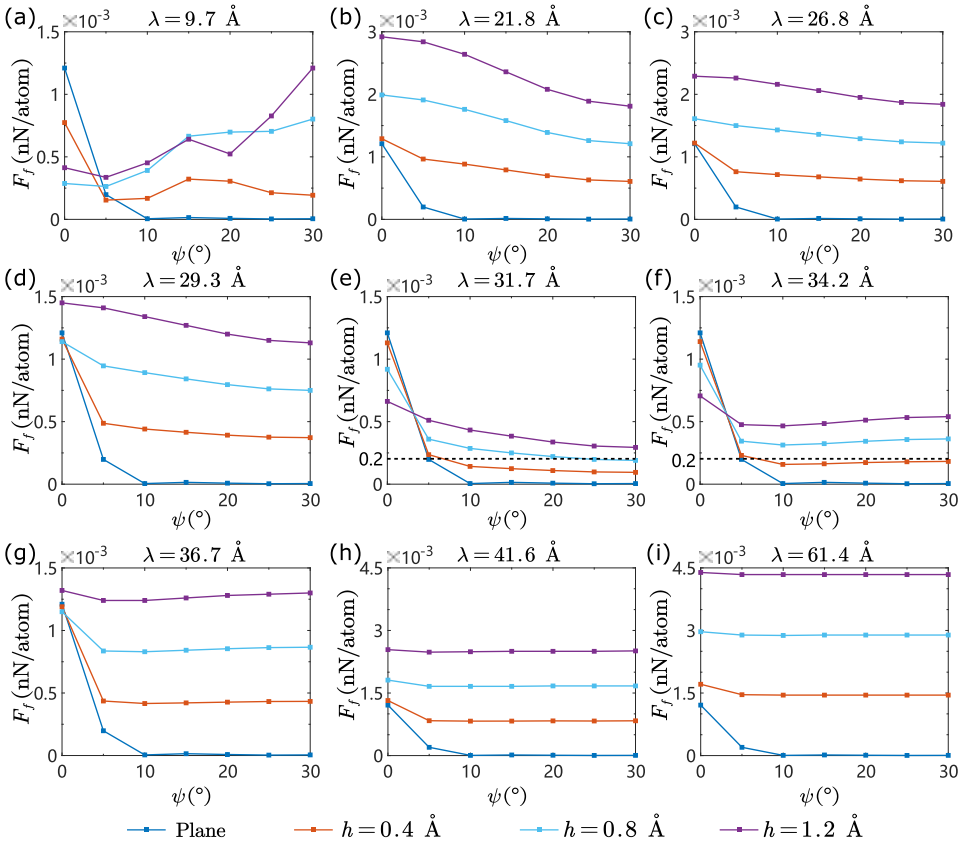

Figure 4: Friction *v.s.* mismatch angle: results based on 9 wavelengths $\lambda = 9.7$ Å, 21.8 Å, 26.8 Å, 29.3 Å, 31.7 Å, 34.2 Å, 36.7 Å, 41.6 Å, and 61.4 Å; and for each wavelength, 4 amplitudes $h = 0$ Å (blue), 0.4 Å (red), 0.8 Å (azure), and 1.2 Å (purple). The flake size $L_x = 41.8$ Å. The dash lines in (e) and (f) indicate the threshold of superlubricity.

We find that despite the interface wrinkles, frictional resistance can still be reduced significantly through contact incommensuration as long as wrinkles remain moderate, as we notice in the case with $\lambda = 31.7$ Å wavelength, structural superlubricity ($F_f < 2.0 \times 10^{-4}$ nN/atom) holds in the presence of wrinkling amplitude 0.4 Å. This observation qualitatively confirms our conjecture on the existence of a tolerance threshold allowing for structural superlubricity on winkled contact interfaces. Moreover, this tolerance threshold can be precisely determined by further refining the design of our simulation cases. And for this purpose, we must also take into account size effect, which might arise from the interplay between the flake and wrinkle's comparative dimensions. We therefore dedicate the next section to determine the tolerance threshold for structural superlubricity, based on the topographic attributes of sliding system.

Tolerance for superlubricity on wrinkled surface with size effect. To examine whether the previous observation presents dependence on the flake size with respect to the wrinkle dimension, we further performed additional two groups of simulations, each resuming the previous scenario but using

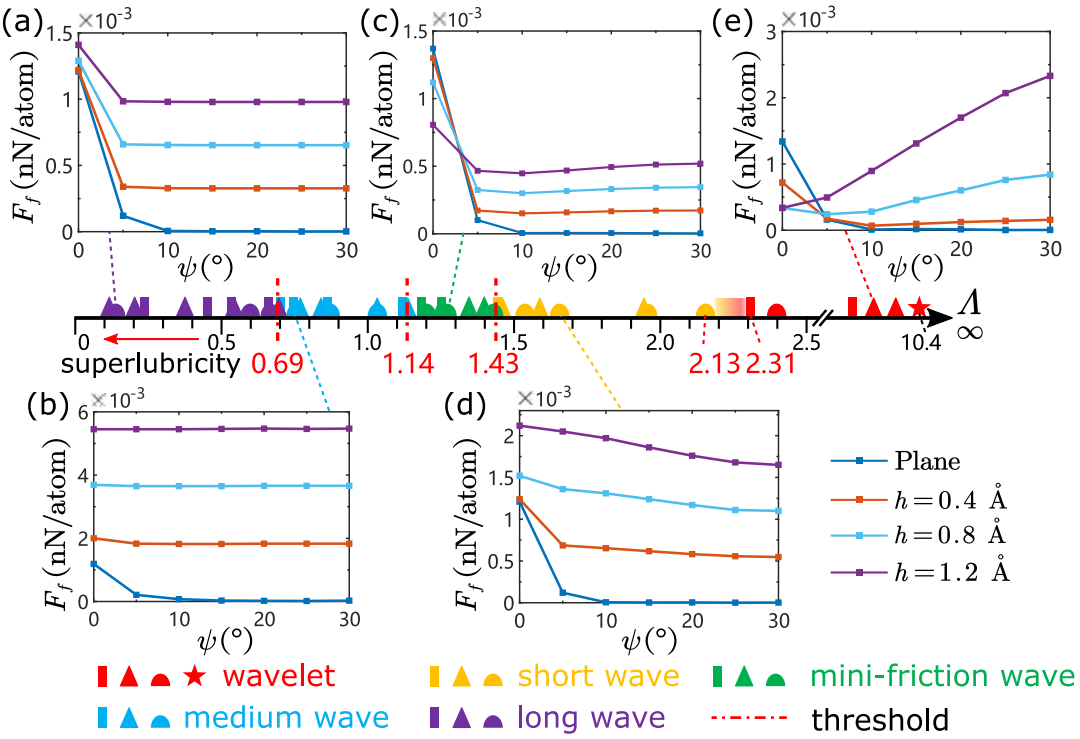

Figure 5: Phase diagram of nanotribology characterized by the dimensionless parameter Λ for different flakes and wrinkled substrates. Five phases with different tribology behavior are observed. The rectangle, triangle, semicircle, and star markers represent the flakes in size of $L_x = 27.1$ Å, 41.8 Å, 51.7 Å, and 100.8 Å, respectively. The markers belonging to different intervals are distinguished by different colors. The parameters in five representative friction states are (a) $\lambda = 474.7$ Å, (b) $\lambda = 31.7$ Å, (c) $\lambda = 41.6$ Å, (d) $\lambda = 31.7$ Å, (e) $\lambda = 11.7$ Å, respectively.

a distinctive flake size. We then considered 3 flake lengths: L_x = 27.1 Å, 41.8 Å and 51.7 Å, with L_x being the characteristic length of the flake. This strategy significantly multiplies the number of simulations, as shown in Fig. 5, but provides us a quantitative insight into the size effect between the flake and the wrinkles. In this regard, we introduce a dimensionless wavelength Λ, defined as the ratio between the flake length L_x and the substrate wavelength λ:

$$\Lambda = \frac{L_x}{\lambda}. \tag{3}$$

For all the cases with distinctive setup of wavelength and the flake size (λ, L_x), we investigate 3 values of undulation amplitude h = 0.4 Å, 0.8 Å and 1.2 Å. Analogous to the dimensionless parameter Λ, we introduce a dimensionless wave amplitude parameter H, which refers to the proportion of wave amplitude h compared to the wavelength λ:

$$H = \frac{h}{\lambda}. \tag{4}$$

Depending on the dimensionless parameter Λ, all the tribological cases can be sorted and classified in two categories. Here, we need to emphasize that the conclusions have been drawn based on our test cases whose undulation amplitude h does not exceed 1.2 Å, which means the upper limit of $H \sim 0.12$ (λ = 9.7 Å, h = 1.2 Å) according to the tested cases. The following observations will hold with certainty within this range.

- **Significant effect of friction reduction with** $\Lambda \in [1.14, 1.43]$. All the cases within this region present significantly friction reduction with increasing mismatch angle, especially in $[5°,\ 30°]$ with incommensurate friction arisen. The superlubric friction can be well preserved in the presence of wrinkling amplitude 0.4 Å. Interestingly, when $\psi = 0°$ (commensurate contact),the commensurate friction force decreases with the rise of wrinkling amplitude. Such phenomenon can be explained by the undulation breaks up the close packing (commensurate contact) of graphene interlayers, thus reduced frictional resistance. For the entire range of mismatch angles and wave amplitudes, friction is weaker than commensurate friction on plane substrate (1.2×10^{-3} nN/atom). Therefore, wrinkles with $\Lambda \in [1.14, 1.43]$ has moderate to negligible deteriorating effect on superlubric friction. Simulations on different normal force F_N show insignificant change of the friction behavior (see Supplementary Material). We have explored the effect of substrate deformations on the friction behavior (see Supplementary Material) and revealed that the substrate elasticity does not qualitatively alter the findings of the present work under moderate normal load. Hod et al. (2018) indicates that edge and pinning effects are important factors for nano tribological behavior with changed flake size. The present work mainly compares the friction behavior with the consistent tribosystem setup, handles the flake and substrate with the same dimension and morphological defaults. Therefore, such edge and pinning effects are not distinct by comparing with the undulation effect.
- **No effect of friction reduction with** $\Lambda \in (0, 1.14] \cup [1.43, \infty]$. In these intervals, mismatch angles no longer lead to reduced friction force and structural superlubricity is not expected to occur. Note that the limit case of $\Lambda \to 0$ refers to the flat state and thus superlubricity is achievable with lattice mismatch.

Some remarks can be drawn based on above observations:

- **Convergence of friction forces with** $\Lambda \in (0, 0.69]$. Friction anisotropy disappears in this region, and friction forces converge to fixed values that exclusively depend on the wave amplitude (see Fig. 7), yet not on the wavelength. When $\Lambda \to 0$, wavelength tends to infinite, which factually refers to an unwrinkled, flat surface configuration.

- **Degraded and irregular friction anisotropy with** $\Lambda \in [0.69, 1.14] \cup [1.43, \infty)$. It refers to regions where friction anisotropy that normally offers reduced friction with angle mismatch disappears. These regions include the very short wavelength region ("wavelet" region in Fig. 5 with large $\Lambda \to \infty$), for which friction tends to increase monotonically with the angle mismatch without superlubricity, and "short" and "medium wave" region in Fig. 5 which lead to the cancellation of friction anisotropy. However, since the level of friction remains considerable, the perspective of superlubricity is ruled out. According to our simulations, a threshold limit is believed to exist between $[2.13, 2.31]$, where such irregular friction anisotropy becomes significant.

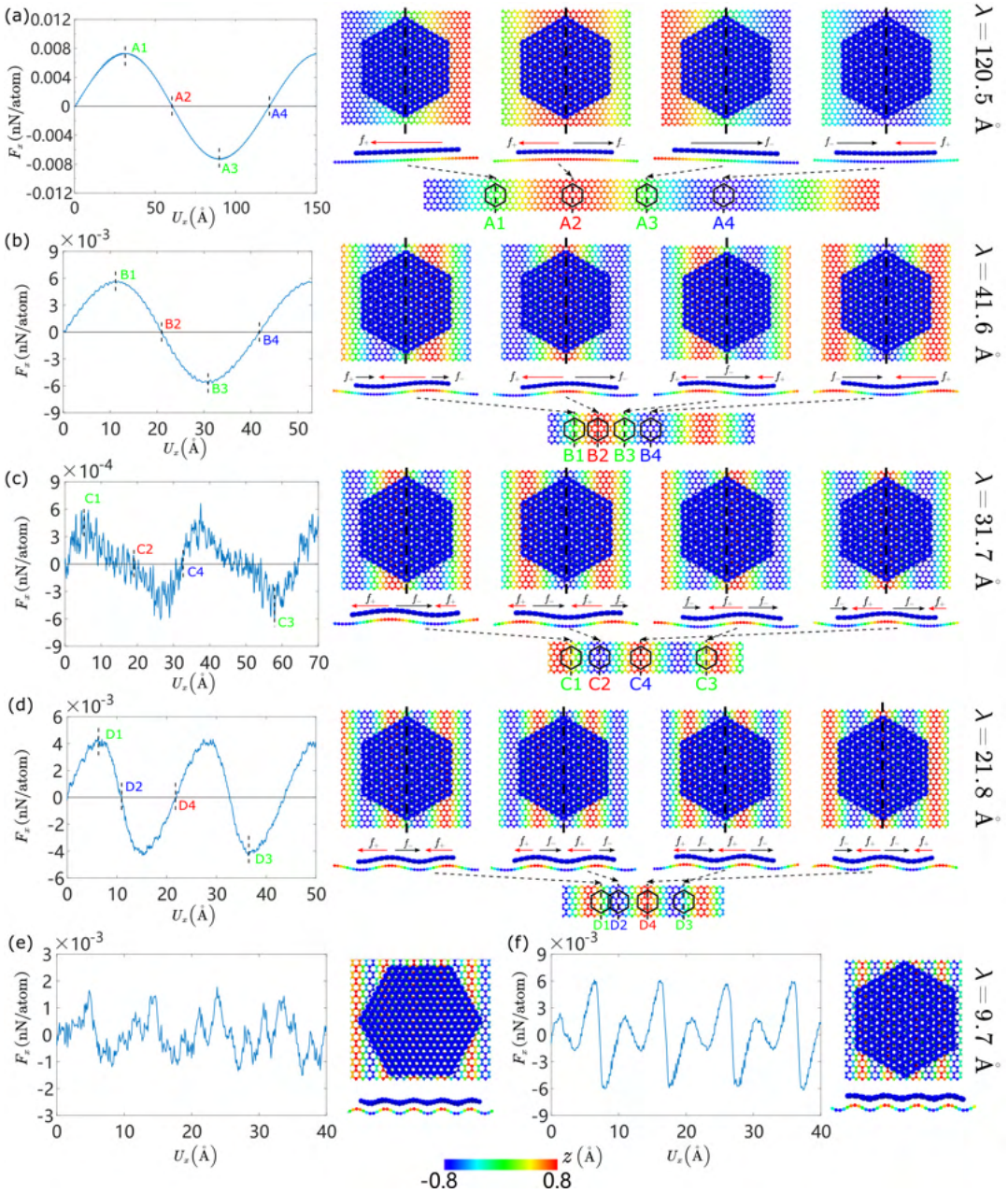

Figure 6: Instantaneous friction forces and corresponding configurations of the graphene flake over wrinkled substrate: (a)-(d) $\psi = 30°$, (e) $\psi = 0°$ and (f) $\psi = 30°$. In simulations, we set $L_x = 41.8$ Å and $h = 0.8$ Å.

We further plot the configuration of the flake and the instantaneous friction forces in Fig. 6, by taking five representative substrates with dimensionless wavelength of different criteria intervals into account. In the long wave interval, the size of the graphene flake is mostly less than half a wavelength. The atoms on the flake at A1 position in Fig. 6(a) are all on the verge of climbing uphill the substrate winkles, with the flake centerline coinciding with the zero point of the wrinkle. At this point, substrate wrinkles uniformly exert resistance forces on the slider atoms. The friction force is observed to reach its maximum. On the contrary, at A3 position in Fig. 6(a), the flake atoms are uniformly moving downhill. Forces they receive from the substrate push them forward, creating the maximum friction force in the negative direction. In comparison, at A2 and A4 position, the centerline of the flake coincides with the peak and valley of the substrate, and the number of atoms moving uphill and downhill the winkles are found to be equal. This fact cancels the total force that the slider atoms receive, and thus creates instantaneously a state of zero friction.

In the medium wave intervals, the substrate undulation that the flake can cover is between half a wave and one wave. When the center line of the flake coincides with the zero-undulation position, the friction reaches its maximum value (B1 position in Fig. 6(b)). The smaller the wavelength, the more atoms located on the downhill. Therefore, the friction force decreases as the wavelength shortens. In the mini-friction wave interval (the dimensionless wavelength $\Lambda \in [1.14,\ 1.43]$), the flake begins to cover a complete wavelength of the substrate winkles, and the canceling effect due to flake atoms simultaneously moving uphill and downhill becomes more obvious. Notably, the instantaneous friction is no longer a sinusoidal wave (Fig. 6(c)), and the position of the least friction appears at position C1 where the flake centerline is found at the zero point of the downhill section. When the wavelength reduces to short wave region, the topographic gradient of the substrate increases, leading to larger friction. The canceling effect due to overlaid atoms moving simultaneously uphill and downhill cannot compensate such increases. Hence, the instantaneous friction presents a sinusoidal wave with relative high amplitude (Fig. 6(d)).

In the wavelet interval, the wrinkling wavelength of the substrate approximates to the length of several lattices. For the commensurate stacking in Fig. 6(e), the total friction force results from the sum of two components. The first component originates from commensurate friction due to cross-lattice movement between the sliding layers. The second one is the result of the substrate undulation. Superposition of the two factors creates a reducing effect, leading to the relatively weak friction observed in the commensurate scenario (Fig. 6(e)). However, with the appearance of contact incommensuration, the friction component due to cross-lattice interaction becomes too weak to offset the component resulting from the substrate undulation. Consequently, the incommensurate friction becomes counter-intuitively more important than the commensurate friction forces within this interval.

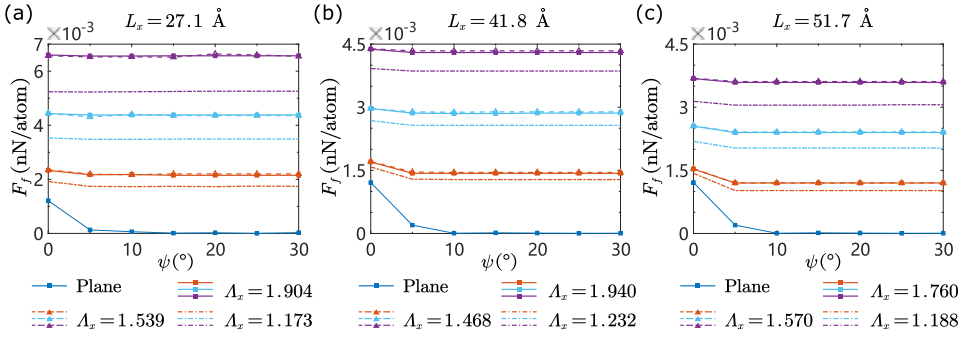

Figure 7: Convergence of friction force for flakes with different sizes: (a) $L_x = 27.1$ Å, (b) $L_x = 41.8$ Å, (c) $L_x = 51.7$ Å. The blue, red, azure and purple lines represent $h = 0$ Å, 0.4 Å, 0.8 Å, and 1.2 Å, respectively.

3.3 Effect of surface topography

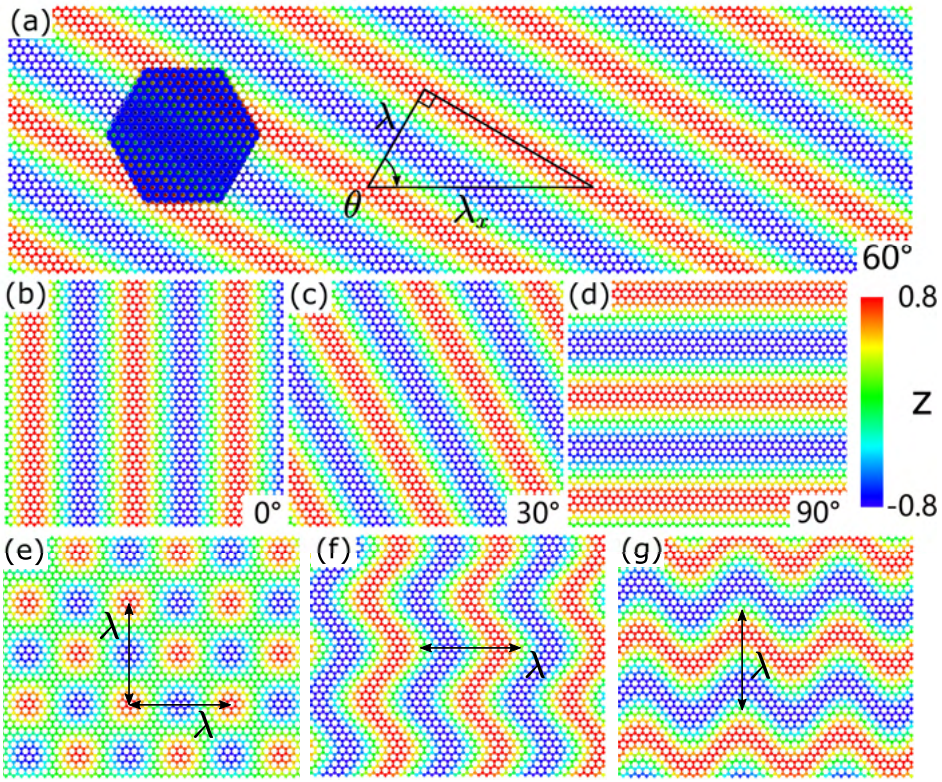

Figure 8: Schematic of topographic patterns: (a)-(c) Wrinkled stripes with different orientations $\theta = 30°$, $60°$ and $90°$, (d) Checkerboard pattern, (e)-(f) Herringbone patterns with different orientations.

Oblique stripes. We now investigate anisotropic frictions on graphene systems with oblique wrinkles whose orientation with respect to x axis forms an angle θ (see in Fig. 8(a)). Similar to the previous modelling protocol, we implement a series of wrinkled substrates with incrementing wrinkle orientation angle θ varying from $0°$ to $90°$. Oscillating friction forces during the sliding process are reported in Fig. 9. It is noticed that the varying wrinkle orientation distinctly modifies the periodicity of friction forces. This is because the effective wavelength is determined by projecting the wrinkling wavelength with respect to x axis (λ_x in Fig. 8(b)), which geometrically evolves with the oblique angle θ. Consequently, when $\theta = 90°$, effective wavelength along x axis approximates to infinite ($\lambda_x \to \infty$), which resembles the flat substrate and leads to the recurrence of incommensurate-induced superlubricity. As shown in Fig. 10, all friction curves for $\theta = 90°$ coincide with the flat substrate counterpart. We then examine the effect of oblique wrinkling wavelength on tribological behavior in Fig. 10, which yields the following conclusions regarding the wrinkle tolerance for superlubricity:

- The regime of regular friction anisotropy is preserved as long as the dimensionless wavelength $\Lambda \in [1.14, 1.43]$.
- Friction reduction by angle mismatch becomes negligible when $\Lambda \in (0.69, 1.14] \cup [1.43, \infty)$.

The above verification confirms our previous findings in a more general framework based on oblique wrinkles.

Checkerboard and herringbone topography. Under biaxial constraint, 2D topographic patterns such as checkerboard and herringbone may emerge in graphene layers. We investigate anisotropic

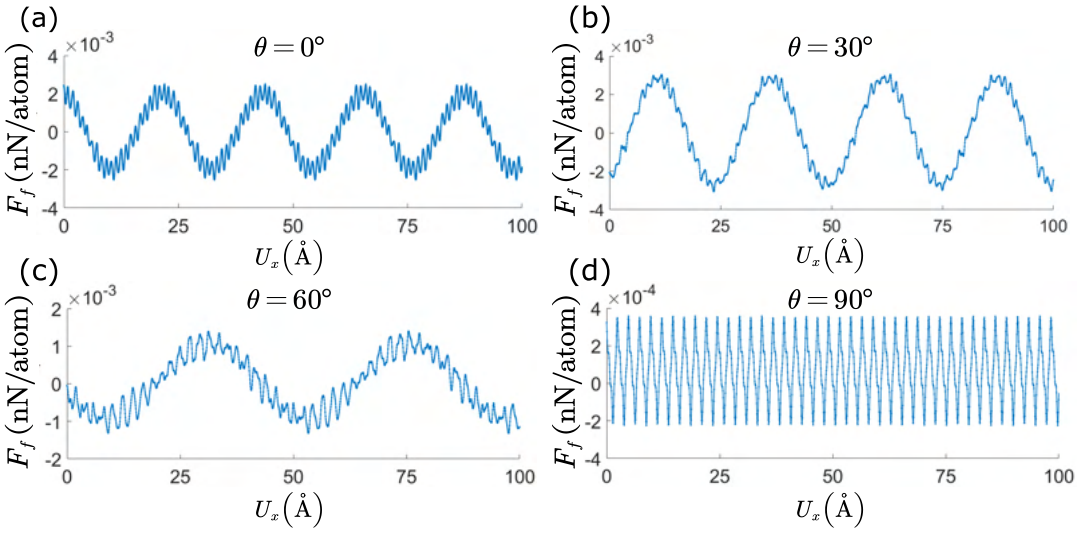

Figure 9: Instantaneous friction force of flakes on wrinkled stripe substrates with different θ = 0°, 30°, 60° and 90°. The frictional periodicity induced by substrate undulations is indicated by the red dash frames. In simulations, we took $L_x = 41.8$ Å, $\lambda = 31.7$ Å, $h = 0.8$ Å and $\psi = 10°$.

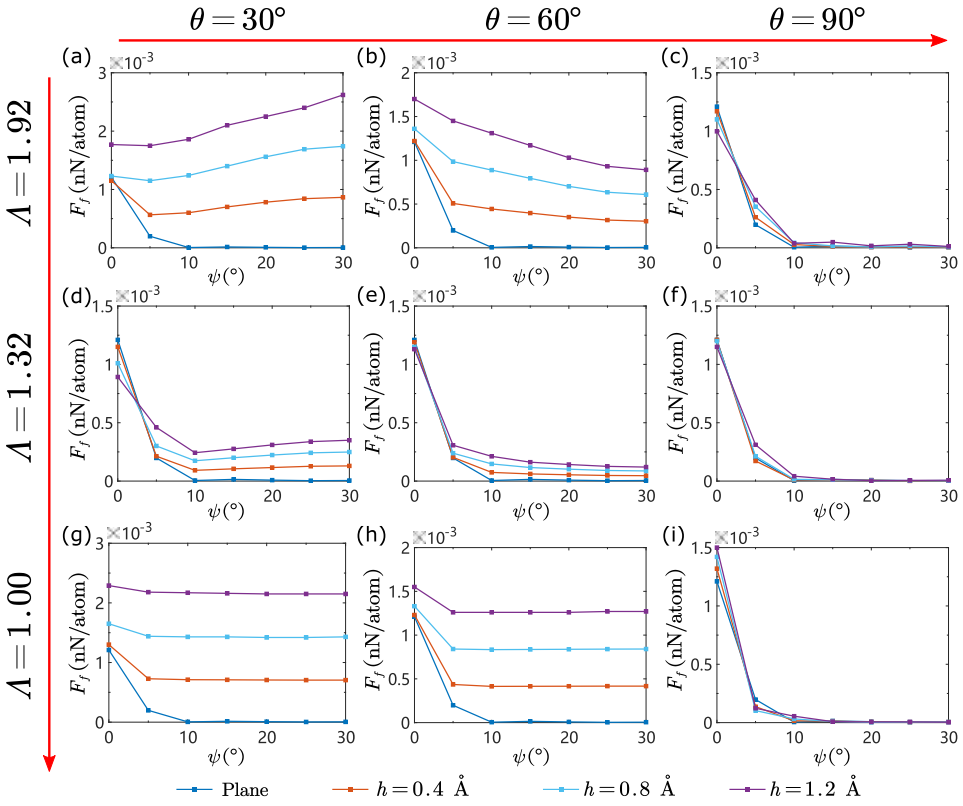

Figure 10: Friction *v.s.* angle mismatch for substrates with different wrinkling directions and dimensionless sizes.

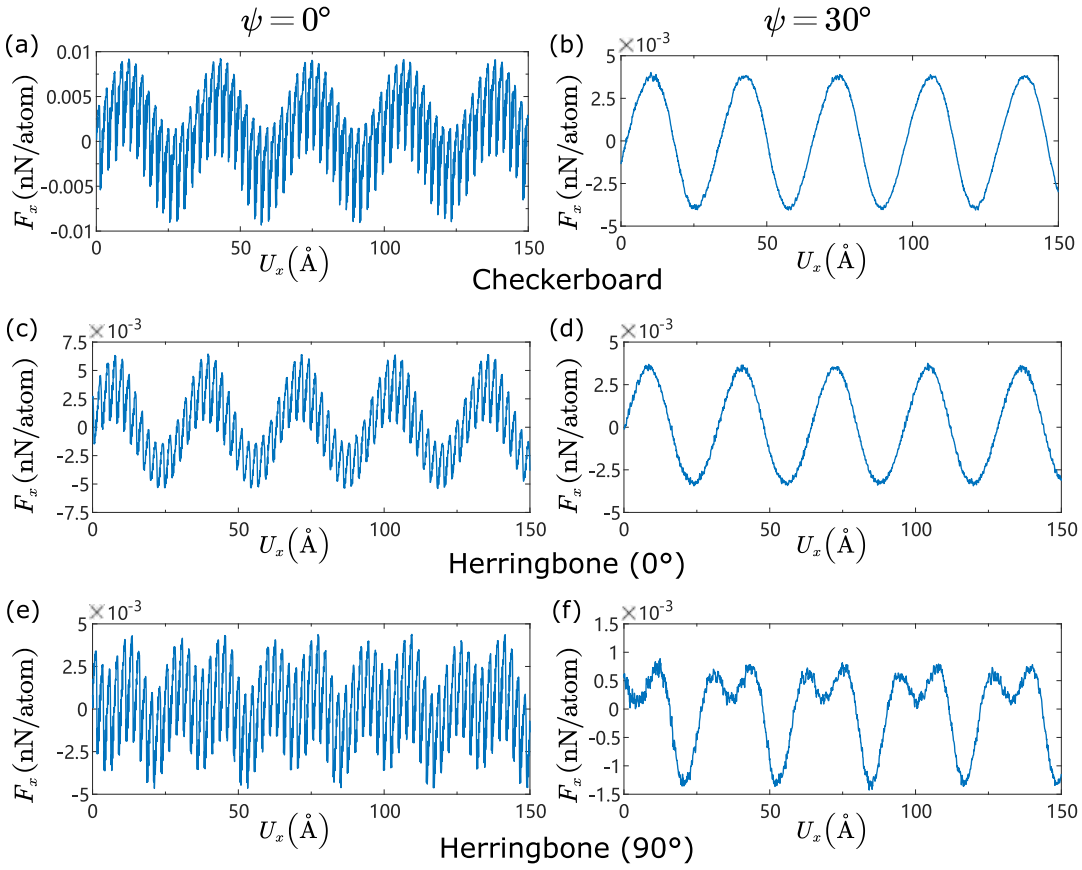

Figure 11: Instantaneous friction force of substrates with different topographies: (a)-(b) Checkerboard, (c)-(d) Herringbone (0°), and (e)-(f) Herringbone (90°). The commensurate mismatch angle (0°) and incommensurate mismatch angle (30°) are plotted for each case.

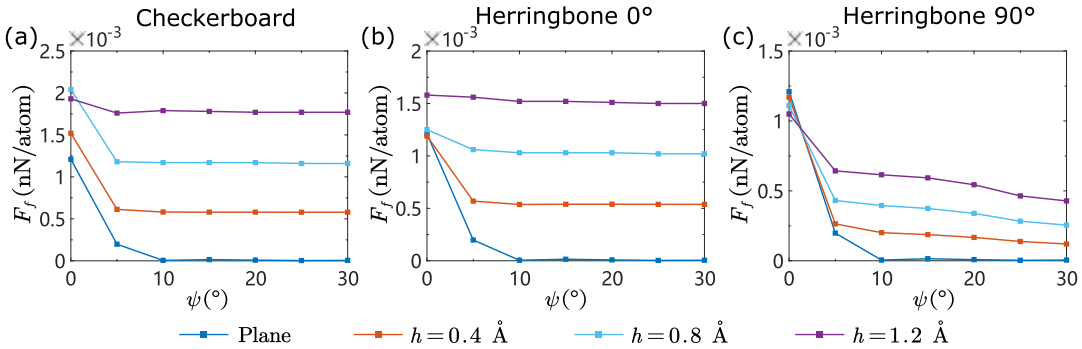

Figure 12: Friction *v.s.* angle mismatch for substrates with different wrinkled patterns: (a) Checkerboard, (c) Herringbone (0°), and (e) Herringbone (90°). In simulations, $\Lambda = 1.32$.

friction on graphene substrates with checkerboard and herringbone patterns (see Fig. 8(e)-(g)). For all substrate setups, we fix dimensionless size $\Lambda = 1.32$ ($\lambda = 31.7$ Å and $L_x = 41.8$ Å), yet vary wrinkle amplitudes $h = 0$ Å, 0.4 Å, 0.8 Å, and 1.2 Å. Since herringbone substrate exhibits directionality, two undulation orientations of 0° and 90° are examined. The instantaneous friction forces during sliding are plotted in Fig. 11. The checkerboard and 0° herringbone topographies indicate a waveform of sinusoidal undulations and cross-lattice movement, yet the 90° herringbone one yields a period-doubling mode. Such waveform is induced by the oblique wrinkles under zigzag direction along the sliding path. We further compare the friction anisotropy in Fig. 12 where low friction with 90° herringbone wrinkles is observed (see Fig. 12(c)). Such surface tribology is similar to the case of $\sim 60°$ oblique wrinkles (see Fig. 8(b)). Yet the wrinkles periodically zigzag along x direction, which leads to moderate increment of the friction. Analogously, the 0° herringbone pattern can be assimilated to $\sim 30°$ wrinkles with zigzag along y direction. The 30° wrinkles suggest larger friction than that of 60° wrinkles (see Fig. 10(d)), and the y direction zigzag makes the friction even larger. Consequently, the 0° herringbone yields relative higher friction with degraded anisotropy. Comparing the three topographies, the highest level of friction force lies in checkerboard substrate (see Fig. 12). Such highest resistance can be interpreted by its undulating morphology which is characterized by isolated peak and valleys in both x and y direction, resulting in the harshest roughness.

4 Concluding remarks

Through abundant simulations based on sliding graphene bilayers on wrinkled graphene systems, we explored effects of surface topography on anisotropic friction. A set of wrinkle tolerance criteria is proposed for predicting the state of friction anisotropy using a geometry-based dimensionless parameter Λ. Notably, the criteria interval $\Lambda \in [1.14, 1.43]$ allows preserving the regime of incommensurate-induced low friction level and even superlubricity with moderate wrinkle amplitude. Beyond this interval, realization of superlubricity becomes improbable due to increased friction force and irregular anisotropy. The sub-interval $\Lambda \in [0.69, 1.14] \cup [1.43, \infty)$ breaks the mechanism of lattice mismatch induced anisotropic friction and repress the regime of superlubricity. Specifically, $\Lambda \in [2.31, \infty)$ results in monotonic increase of friction forces. Friction forces converge to fixed values that exclusively depend on the wave amplitude regardless of the wavelength as $\Lambda \in (0, 0.69]$, and the particular case of $\Lambda \to 0$ covers the friction on a plane surface. We investigated the influence of diverse topographies including oblique stripes, checkerboard and herringbone patterns, which revealed larger friction compared with that of sinusoidal undulations. The results can be viewed as a step forward towards quantitative understanding of microscopic superlubricity on wrinkled graphene, and contribute to the scaling-up effort on advancing superlubricity to realistic applications with practical roughness topographies.

Acknowledgements

This work is supported by the National Natural Science Foundation of China (Grants No. 11872150 and 11890673), Shanghai Rising-Star Program (Grant No. 19QA1400500), Shanghai Chenguang Program (Grant No. 16CG01), and State Key Laboratory for Strength and Vibration of Mechanical Structures (Grant No. SV2018-KF-17).

References

Almeida, C.M., Prioli, R., Fragneaud, B., Cançado, L.G., Paupitz, R., Galvão, D.S., De Cicco, M., Menezes, M.G., Achete, C.A., Capaz, R.B., 2016. Giant and tunable anisotropy of nanoscale friction in graphene. Sci. Rep. 6, 31569-1–31569-9.

Bonelli, F., Manini, N., Cadelano, E., Colombo, L. 2009. Atomistic simulations of the sliding friction of graphene flakes. Eur. Phys. J. B 70, 449–459.

Cho, D.-H., Wang, L., Kim, J.-S., Lee, G.-H., Kim, E.S., Lee, S., Lee, S.Y., Hone, J., Lee, C. 2013. Effect of surface morphology on friction of graphene on various substrates. Nanoscale 5, 3063–3069.

Choi, J.S., Kim, J.-S., Byun, I.-S., Lee, D.H., Lee, M.J., Park, B.H., Lee, C., Yoon, D., Cheong, H., Lee, K.H., Son, Y.-W., Park, J.Y., Salmeron, M., 2011. Friction anisotropy-driven domain imaging on exfoliated monolayer graphene. Science 333, 607–610.

de Wijn, A.S., Fusco, C., Fasolino, A., 2010. Stability of superlubric sliding on graphite. Phys. Rev. E 81, 046105-1–046105-11.

Deng, S., Berry, V., 2016. Wrinkled, rippled and crumpled graphene: an overview of formation mechanism, electronic properties, and applications. Mater. Today 19, 197–212.

Dienwiebel, M., Verhoeven, G.S., Pradeep, N., Frenken, J.W.M., Heimberg, J.A., Zandbergen, H.W., 2004. Superlubricity of Graphite. Phys. Rev. Lett. 92, 126101-1–126101-4.

Filippov, A.E., Dienwiebel, M., Frenken, J.W.M., Klafter, J., Urbakh, M., 2008. Torque and Twist against Superlubricity. Phys. Rev. Lett. 100, 046102-1–046102-4.

Guo, Y., Guo, W., 2013. Soliton-like thermophoresis of graphene wrinkles. Nanoscale 5, 318–323.

Hirano, M., Shinjo, K., Kaneko, R., Murata, Y., 1991. Anisotropy of frictional forces in muscovite mica. Phys. Rev. Lett. 67, 2642–2645.

Hirano, M., Shinjo, K., 1993. Superlubricity and frictional anisotropy. Wear 168, 121–125.

Hod, O., Meyer, E., Zheng, Q., Urbakh, M., 2018. Structural superlubricity and ultralow friction across the length scales. Nature 563, 485–492.

Lennard-Jones, J.E., 1931. Cohesion. Proc. Phys. Soc. 43, 461–482.

Leven, I., Krepel, D., Shemesh, O., Hod, O., 2012. Robust Superlubricity in graphene/h-BN heterojunctions. J. Phys. Chem. Lett. 4, 115–120.

Li, Q., Liu, X.-Z., Kim, S.-P., Shenoy, V.B., Sheehan, P.E., Robinson, J.T., Carpick, R.W. 2014. Fluorination of graphene enhances friction due to increased corrugation. Nano Lett. 14, 5212–5217.

Liu, Y., Grey, F., Zheng, Q., 2014. The high-speed sliding friction of graphene and novel routes to persistent superlubricity. Sci. Rep. 4, 4875-1–4875-7.

Liu, Z., Yang, J., Grey, F., Liu, J.Z., Liu, Y., Wang, Y., Yang, Y., Cheng, Y., Zheng, Q., 2012. Observation of microscale superlubricity in graphite. Phys. Rev. Lett. 108, 205503-1–205503-5.

Mandelli, D., Leven, I., Hod, O., Urbakh, M., 2017. Sliding friction of graphene/hexagonal-boron nitride heterojunctions: a route to robust superlubricity. Sci. Rep. 7, 10851-1–10851-10.

Martin, J.M., Donnet, C., Le Mogne, Th., Epicier, Th., 1993. Superlubricity of molybdenum disulphide. Phys. Rev. B 48, 10583–10586.

Meyer, J.C., Geim, A.K., Katsnelson, M.I., Novoselov, K.S., Booth, T.J., Roth, S., 2007. The structure of suspended graphene sheets. Nature 446, 60–63.

Obraztsov, A.N., Obraztsova, E.A., Tyurnina, A.V., Zolotukhin, A.A., 2007. Chemical vapor deposition of thin graphite films of nanometer thickness. Carbon 45, 2017–2021.

Ouyang, W., de Wijn, A.S., Urbakh, M., 2018. Atomic-scale sliding friction on a contaminated surface. Nanoscale 11, 2186-2193.

Pan, F., Wang, R., Liu, L., Chen, Y., Zhang, Z., 2019. Bending induced interlayer shearing, rippling and kink buckling of multilayered graphene sheets. J. Mech. Phys. Solids 122, 340–363.

Paronyan, T.M., Pigos, E.M., Chen, G. Harutyunyan, A.R., 2011. Formation of ripples in graphene as a result of interfacial instabilities. ACS Nano 5, 9619–9627.

Plimpton, S., 1995. Fast parallel algorithms for short-range molecular dynamics. J. Comput. Phys. 117, 1–19.

Smolyanitsky, A., 2015. Effects of thermal rippling on the frictional properties of free-standing graphene. RSC Adv. 5, 29179–29184.

Socoliuc, A., Bennewitz, R., Gnecco, E., Meyer, E., 2004. Transition from stick-slip to continuous sliding in atomic friction: entering a new regime of ultralow friction. Phys. Rev. Lett. 92, 134301-1–134301-4.

Stuart, S.J., Tutein, A.B., Harrison, J.A., 2000. A reactive potential for hydrocarbons with intermolecular interactions. J. Chem. Phys. 112, 6472–6486.

van Wijk, M.M., Dienwiebel, M., Frenken, J.W.M., Fasolino, A., 2013. Superlubric to stick-slip sliding of incommensurate graphene flakes on graphite. Phys. Rev. B 88, 235423-1–235423-7.

Wang, K., Ouyang, W., Cao, W., Ma, M., Zheng, Q., 2019. Robust superlubricity by strain engineering. Nanoscale 11, 2186–2193.

Wang, K., Qu, C., Wang, J., Ouyang, W., Ma, M., Zheng, Q., 2019. Strain engineering modulates graphene interlayer friction by moiré pattern evolution. ACS Appl. Mater. & Inter. 11, 36169–36176.

Wang, L.-F., Ma, T.-B., Hu, Y.-Z., Zheng, Q., Wang, H., Luo, J., 2014. Superlubricity of two-dimensional fluorographene/MoS_2 heterostructure: a first-principles study. Nanotechnology 25, 385701-1–385701-6.

Wang, W., Shen, J., He, Q.-C., 2019. Microscale superlubricity of graphite under various twist angles. Phys. Rev. B 99, 054103-1–054103-7.

Zhang, H., Guo, Z., Gao, H., Chang, T., 2015. Stiffness-dependent interlayer friction of graphene. Carbon 94, 60-66.

Zhang, S., Hou, Y., Li, S., Liu, L., Zhang, Z., Feng, X.-Q., Li, Q., 2019. Tuning friction to a superlubric state via in-plane straining. Proc. Natl. Acad. Sci. U.S.A. 116, 24452–24456.

Supplementary Material for "Effect of surface topography on anisotropic friction of graphene layers"

Mingda Ding,[1] Yu Cong,[2] Ruiyang Li,[1] and Fan Xu[1,*]

[1] *Institute of Mechanics and Computational Engineering, Department of Aeronautics and Astronautics, Fudan University, Shanghai 200433, P.R. China*

[2] *Université Paris-Saclay, Univ Evry, LMEE, 91020, Evry, France*

(Dated: August 25, 2020)

* Corresponding author.

fanxu@fudan.edu.cn (F. Xu)

Here we provide more details on the selection of interlayer potential, pulling spring stiffness k_{link} and sliding velocity v_{pull}, and discussions on effect of normal load F_N and substrate elasticity on friction behavior.

I. THE CHOICE OF POTENTIAL MODEL FOR INTERLAYER INTERACTIONS

To choose the potential model for graphene interlayer behaviors, both Lennard-Jones (LJ) and Kolmogorov-Crespi (KC) potentials [1] had been examined prior to our investigations. Tests had been performed on a set of benchmarks whose results are reported in Fig. S1. In these cases, we compared friction anisotropy with varying wavelengths and amplitudes, using both LJ and KC potentials. We tested the KC potential based on models with 3 wavelengths $\lambda = 21.8$ Å ($\Lambda = 1.92$), 34.2 Å ($\Lambda = 1.22$), and 61.4 Å ($\Lambda = 0.68$), then for each wavelength, 4 amplitudes $h = 0$ Å, 0.4 Å, 0.8 Å, and 1.2 Å. In these cases, we observed similar relationship between friction and wavelength as those obtained with LJ potential, with an obvious reduction of friction with $\lambda = 34.2$ Å (see Figs. 4(b)(f)(i) in the main text). The low friction wavelength is retained for KC potential as well. An obvious increment in friction is also observed with lattice mismatch $\psi \in [5°, 30°]$ and $\lambda = 21.8$ and 61.4 Å. Notably, the KC potential describes an extremely strong friction with 0° lattice mismatch (commensurate cases) as reported in [2].

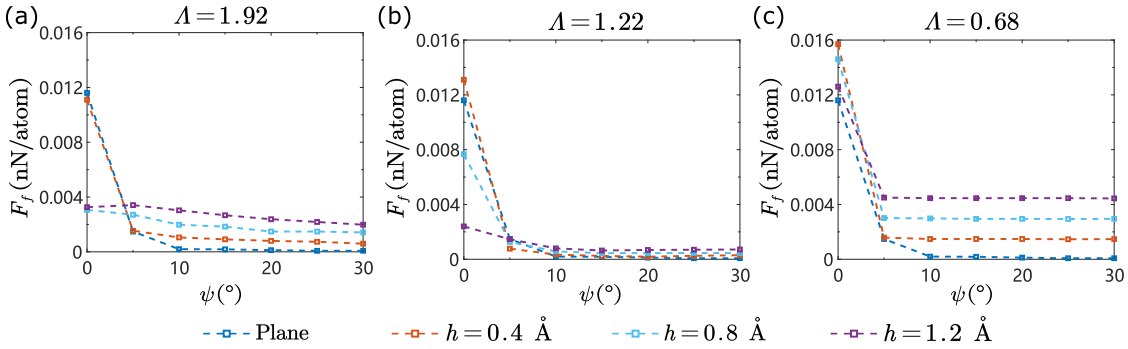

FIG. S1. Friction anisotropy studied with Kolmogorov-Crespi (KC) potential for interlayer interactions: friction *v.s.* mismatch angle. (a) $\Lambda = 1.92$, (b) $\Lambda = 1.22$, (c) $\Lambda = 0.68$. Four amplitudes $h = 0$ Å (blue), 0.4 Å (red), 0.8 Å (azure) and 1.2 Å (purple) are taken into account. The flake size $L_x = 41.8$ Å.

According to [3], the original KC potential presents imperfection in correctly assessing

interactions in AA and AB stacking states. For the reasons stated above, we preferred LJ potential for both its capacity of representing the intended phenomenon, *i.e.,* friction anisotropy, and its higher computational efficiency given the extensive amount of cases needed for this study.

II. EFFECT OF PULLING SPRING CONSTANT $K_{\mathbf{link}}$ AND STICK-SLIP BEHAVIOR ON FRICTION BEHAVIOR

We have performed further simulations to examine the effect of spring constant of the pulling spring connected between the nanoflake's centroid and the prescribed movement on friction behavior. We reveal that the stick-slip behavior exists on two levels, *i.e.,* wrinkle level and lattice level.

A weak spring constant leads to a wrinkle-level stick-slip behavior. We examined the spring constant $k_{\text{link}} = 3.63$ N/m which is one order of magnitude smaller than the present stiffness (36.3 N/m). We took three representative wavelength $\lambda = 21.8$ Å, 31.7 Å, and 61.4 Å from the critical dimensionless intervals in phase diagram with $h = 0.8$ Å and $L_x = 41.8$ Å. The instantaneous friction forces and displacements of flake centroid are plotted in Fig. S2. One can constantly observe stick-slip movement with weaker spring stiffness $k_{\text{link}} = 3.63$ N/m for all the wavelengths and mismatch angles (see Fig. S2(a)-(f)), especially for $\lambda = 21.8$ Å and 61.4 Å because of relatively larger friction forces. The wavelength $\lambda = 31.7$ Å belongs to the criteria interval [1.14, 1.43] in which low friction is preserved. In Fig. S2(g)-(i), the displacements of the flake as a function of simulation time are plotted. The zigzag curves (purple and blue) suggest that the flakes with weaker pulling spring first move with a relatively slow speed and suddenly speed up to jump over an energy barrier, while the flakes with $k_{\text{link}} = 36.3$ N/m (red and azure dash lines) move at a uniform speed without stick-slip behavior. The periodicity of the zigzag curves is consistent with the substrate wavelength. When $\lambda = 31.7$ Å, the stick-slip response becomes insignificant due to low friction force.

Such wrinkle level stick-slip can be explained by the classical Prandt-Tomlinson (PT) model [4], also applied in [5]. The sliding continuity depends on the dimensionless parameter:

$$\eta = \frac{4\pi^2 U_\lambda}{k_{\text{link}} \lambda^2}, \tag{S1}$$

where U_λ is the wave potential amplitude and λ denotes substrate wavelength. Small value of η indicates a continuous friction, while large value of η leads to stick-slip sliding. One can see that weaker spring stiffness yields larger η and thus leads to stick-slip behavior.

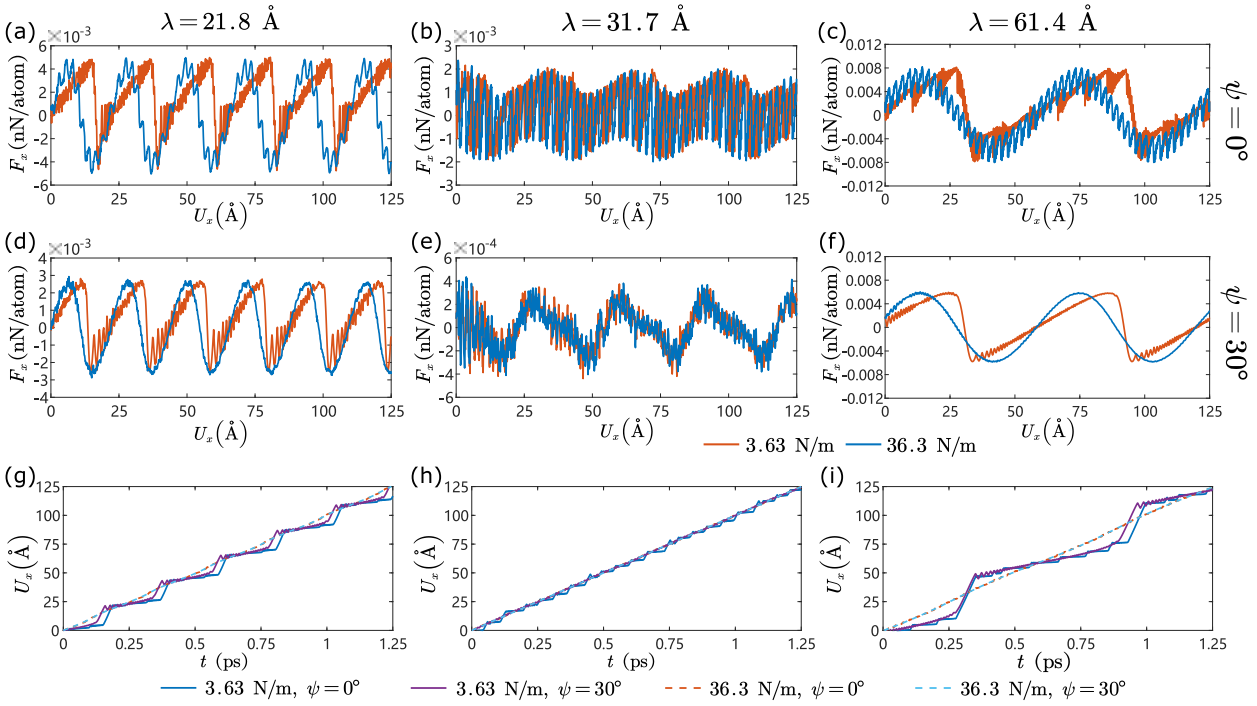

FIG. S2. Effect of pulling spring stiffness k_{link} on friction response. (a)-(f) Instantaneous friction forces for different setups of spring stiffness, wavelength, and mismatch angle (commensurate (a)-(c) $\psi = 0°$ and incommensurate (d)-(f) $\psi = 30°$), amplitude $h = 0.8$ Å. (g)-(i) Motion of the flake centroid *v.s.* simulation time.

A typical lattice-level stick-slip behavior with commensurate friction is shown in Fig. 3(a) and (e) in the main text. The incommensurate friction does not demonstrate such stick-slip phenomenon, with a combination of cross-lattice movement and thermal fluctuation instead. According to the widely used Frenkel-Kontorova (FK) model [6], a bilayer tribological system is modelled by a chain of elastically linked atoms submitted to a periodic potential due to the substrate atoms. The sliding movement of the atom chain (representing the slider) on the substrate can be either continuous or stick-slip, depending on a dimensionless parameter:

$$\lambda^{FK} = \frac{4\pi^2 U_a}{k_{\text{chain}} a^2}, \tag{S2}$$

where U_a is the substrate potential amplitude, a denotes lattice constant, and k_{chain} is the stiffness of the inter atoms. For large λ^{FK}, the friction is dissipative with stick-slip

behavior, while small λ^{FK} yields continuous sliding. In the cases of commensurate stacking, larger U_a with high friction force induces a stick-slip sliding, while the incommensurate stacking with smaller U_a (low friction force) yields continuous sliding. Notably, the effective spring constant within the FK framework corresponds to the tensional elastic stiffness of graphene C-C chain, whose value is $k_{\text{chain}} = 26.6\,\text{eV/Å}^2 \approx 426.1$ N/m [7]. The pulling spring constant $k_{\text{link}} = 36.3$ N/m in the present work, experimentally chosen as the lateral stiffness of the FFM (Friction Force Microscope) tip in reality, is much smaller than the value of graphene C-C chain. Such spring stiffness should not surpass the in-plane stiffness of graphene ($340 \sim 426.1$ N/m)[8].

In general, a weak pulling spring leads to a slick-slip behavior, while its influence on the friction remains quantitatively limited. Furthermore, low friction is preserved with the wavelength in the criteria interval [1.14, 1.43].

III. EFFECT OF NORMAL FORCE F_N AND SLIDING VELOCITY v_{pull} ON FRICTION

The normal load F_N and sliding velocity v_{pull} used in the present work are chosen from the literature, the values of which have been widely used in nanotribology simulations [9, 10]. In [9], normal loads for modelling interlayer interactions are usually set in the interval $F_N \in [0,\ 0.6]$ nN/atom. When $F_N > 0.6$ nN, a sudden increase in friction may arise from high dissipative stick-slip regime, which is unexpected in superlubricity [11]. We have further tested complementary settings with the normal load set to F_N = 0.1 nN/atom, 0.2nN/atom and 0.3 nN/atom, and we report the results in Fig. S3. Simulations on different F_N shows no qualitative modification of the friction behavior, observation confirmed by 3 dimensionless wavelengths (1.92, 1.22 and 0.68). Quantitatively, smaller F_N leads to smaller friction.

Concerning the sliding velocity prescribed to the nanoflake v_{pull}, we recognize that the velocity range of $4.84 \sim 100$ m/s is widely considered in the literature [11–13]. We have further tested other pulling velocities and the results are shown in Fig. S4. In simulations, both commensurate ($\psi = 0°$) and incommensurate ($\psi = 30°$) stacking are considered. One can see that all the friction forces are consistent.

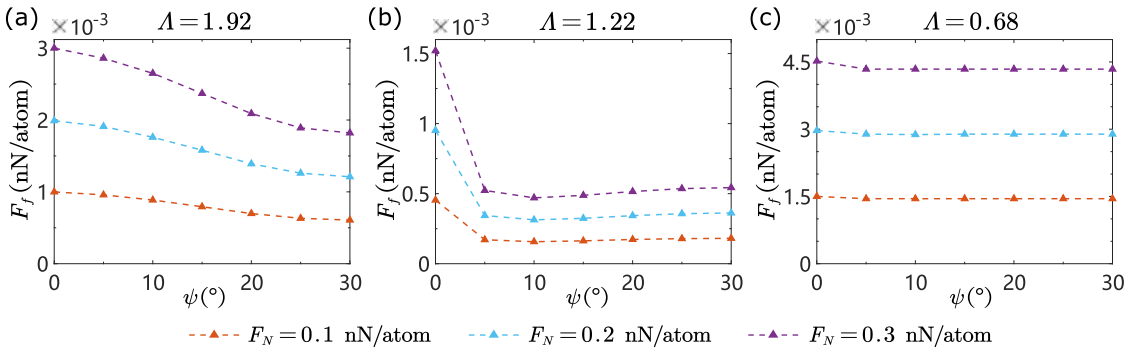

FIG. S3. Influence of the normal force F_N with varying mismatch angles on friction response: (a) $\Lambda = 1.92$, (b) $\Lambda = 1.22$, (c) $\Lambda = 0.68$. The wave amplitudes $h = 0.8$ Å and flake size $L_x = 41.8$ Å. The normal load F_N are set 0.1 nN/atom (red), 0.2 nN/atom (azure), and 0.3 nN/atom (purple), respectively.

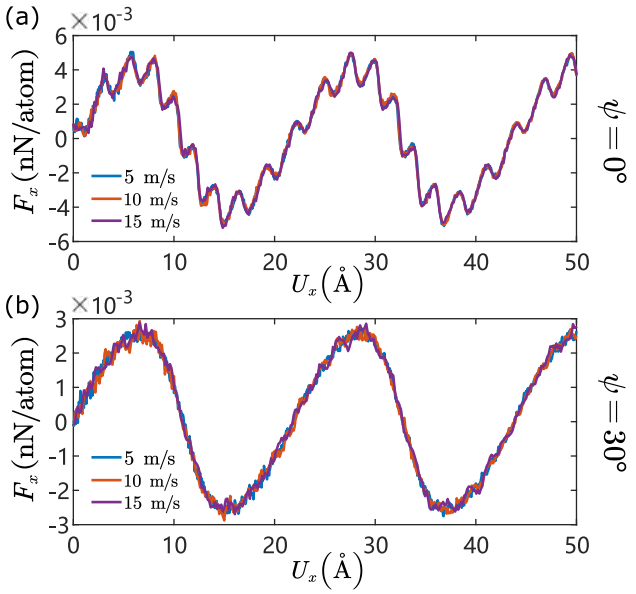

FIG. S4. Influence of prescribed sliding velocity v_{pull} on instantaneous friction behavior: (a) Commensurate ($\psi = 0°$) and (b) Incommensurate ($\psi = 30°$) stacking. In simulations, we took $\lambda = 31.7$ Å, $h = 0.8$ Å and $L_x = 41.8$ Å.

IV. EFFECT OF SUBSTRATE ELASTICITY ON FRICTION BEHAVIOR

In the present model the flake atoms are free in x and z direction (force load is prescribed in x direction instead of displacement load), and we constrain the displacement of the atoms in y direction. Such constraints are imposed to exclude the translational movement along

y direction and rotation along z axis, allowing the in-plane (x direction) and out-of-plane (z axis) elasticity while maintaining the stacking and mismatch configuration. In this way, elasticity of the nanoflake is taken into account.

During the sliding process, the substrate may also deform due to the important normal load. In this regard, we further performed verification simulations which also account for the substrate elasticity. Here, to model the substrate deformation, each substrate atom is connected to its initial position via a spring along the z direction. The stiffness $k_{\text{sub}} = 2.7$ N/m which is equivalent to the theoretical spring stiffness between two graphene layers, calculated with the well-known theory of Hamaker summation. Thus, every substrate atom is free to move elastically along z under the effect of the foundation spring. Then, the centroid atom of the substrate is fixed along x and y directions. Periodic conditions are prescribed on the substrate boundary edges. Other model parameters and boundary conditions are identical to the model without the foundation spring. We considered a nanoflake of size $L_x = 41.8$ Å and selected 3 representative substrate configurations with wavelength $\lambda = 21.8$ Å, 34.2 Å and 61.4 Å (or $\Lambda = 1.92, 1.22$ and 0.68, in terms of the dimensionless wavelength).

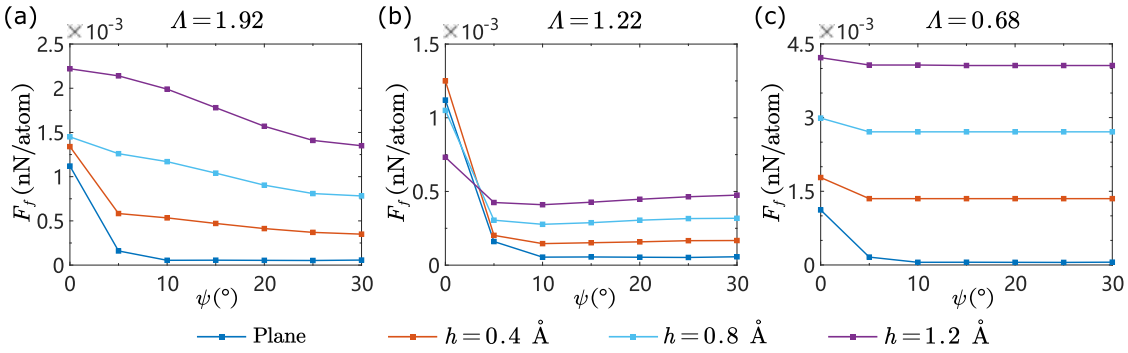

FIG. S5. Effect of the substrate elasticity on friction anisotropy: friction forces *v.s.* mismatch angle. (a) $\Lambda = 1.92$, (b) $\Lambda = 1.22$, (c) $\Lambda = 0.68$. Four amplitudes $h = 0$ Å (blue), 0.4 Å (red), 0.8 Å (azure) and 1.2 Å (purple) are considered. The flake size $L_x = 41.8$ Å.

Results are reported in Fig. S5. One can observe significantly reduced friction with $\lambda = 34.2$ Å which is consistent with Fig. 4 in the main text. The deformable substrate with $\lambda = 21.8$ Å and 61.4 Å showed no friction reduction with weak anisotropy, which matches the result of Fig. 4 in the main text, although admittedly, existing literature did reveal influence on the friction behavior by substrate stiffness [14]. In this regard, further effort is required to better comprehend tribological effects of substrate elasticity.

We admit that very large normal load may lead to substrate deformations, but in the present investigation, the normal load remains moderate. The assumption of rigid substrate is thus rational and the neglection of the substrate deformation does not change the conclusion of the present work.

---

[1] Kolmogorov, A.N., Crespi, V., 2005. Registry-dependent interlayer potential for graphitic systems. Phys. Rev. B 71, 235415-1–235415-6.

[2] Pan, F., Wang, R., Liu, L., Chen, Y., Zhang, Z., 2019. Bending induced interlayer shearing, rippling and kink buckling of multilayered graphene sheets. J. Mech. Phys. Solids 122, 340–363.

[3] Wen, M., Carr, S., Fang, S., Kaxiras, E., Tadmor, E. B., 2018. Dihedral-angle-corrected registry-dependent interlayer potential for multilayer graphene structures. Phys. Rev. B 98, 235404-1–235404-11.

[4] Prandtl, L., 1928. L. Prandtl, Ein Gedankenmodell zur kinetischen Theorie der festen Körper. Z. Angew. Math. Mech. 8, 85-106.

[5] Socoliuc, A., Bennewitz, R., Gnecco, E., Meyer, E., 2004. Transition from stick-slip to continuous sliding in atomic friction: entering a new regime of ultralow friction. Phys. Rev. Lett. 92, 134301-1–134301-4.

[6] Braun, O. M., Kivshar, Y. S., 2004. The Frenkel-Kontorova model: concepts, methods, and applications. Springer 1-472.

[7] Zhang, D.-B., Akatyeva, E., Dumitrică, T., 2011. Bending Ultrathin Graphene at the Margins of Continuum Mechanics. Phys. Rev. Lett. 106, 255503.

[8] Lee, C., Wei, X., Kysar, J. W., Hone, J., 2008. Measurement of the elastic properties and intrinsic strength of monolayer graphene. Science 321, 385–388.

[9] Vu, C. C., Zhang, S., Urbakh, M., Li, Q., He, Q.-C., Zheng, Q., 2016. Observation of normal-force-independent superlubricity in mesoscopic graphite contacts. Phys. Rev. B 94, 081405(R).

[10] Wang, K., Ouyang, W., Cao, W., Ma, M., Zheng, Q., 2019. Robust superlubricity by strain engineering. Nanoscale 11, 2186–2193.

[11] van Wijk, M.M., Dienwiebel, M., Frenken, J.W.M., Fasolino, A., 2013. Superlubric to stick-slip sliding of incommensurate graphene flakes on graphite. Phys. Rev. B 88, 235423.

[12] Wang, K., Qu, C. Wang, J., Quan, B., Zheng, Q., 2020. Characterization of a microscale

superlubric graphite interface. Phys. Rev. Lett. 125, 026101-1–026101-6.

[13] Onodera, T. , Morita, Y., Nagumo, R., Miura, R., Suzuki, A., Tsuboi, H., Hatakeyama, N., Endou, A., Takaba, H., Dassenoy, F., Minfray, C., Joly-Pottuz, L., Kubo, M., Martin, J.-M., Miyamoto, A., 2010. A computational chemistry study on friction of h-MoS2. Part II. Friction anisotropy. J. Phys. Chem. B 114, 15832–15838.

[14] Zhang, H., Guo, Z., Gao, H., Chang, T., 2015. Stiffness-dependent interlayer friction of graphene. Carbon 94, 60-66.